RESEARCH ARTICLE

Energy & Environmental Materials WILEY

Electrocatalysis

Enhanced Urea Oxidation Reaction by Mn-Doped Nickel Hydroxide From Wastewater

Filippo Bano, Da Chen, Daniele Perilli, Samuele Zambonin, Dario Mosconi, Marco Roverso, Veronica Celorrio, Cristiana Di Valentin, and Laura Calvillo**

Integrating urea electrolysis into wastewater treatment systems represents a promising strategy to couple hydrogen production with environmental remediation. Nickel-based materials are among the most efficient non-precious catalysts for the urea oxidation reaction under alkaline conditions, yet Ni scarcity and its potential toxicity call for more sustainable alternatives. After demonstrating that Ni hydroxide recovered from wastewater is a good urea oxidation reaction catalyst, in this work, we report a fundamental and systematic study about urea oxidation reaction catalysts based on manganese-doped nickel hydroxide obtained through a synthesis route that mimics Ni recovery from wastewater to enhance the urea oxidation reaction performance. Thus, it offers both catalytic performance and circular-material benefits. A comprehensive characterization of the $Ni(OH)_2$-based materials by experimental techniques, such as X-ray diffraction, scanning electron microscopy, X-ray absorption, and X-ray photoemission spectroscopy, combined with DFT theoretical calculations has revealed that Mn incorporation modifies the hydroxide structure, introduces ions in the +3 oxidation state, and promotes the formation of catalytically active NiOOH species. Mn dopants induce a favorable electronic effect through an indirect participation in the urea oxidation reaction mechanism involving oxidation state variation but not direct chemical bond formation. The reaction intermediates are in part different from those reported in previous literature. At a given potential, Mn doping enhances the overall urea oxidation rate, resulting in increased hydrogen evolution at the cathode. These findings point to a novel mechanistic understanding of the Mn-dopant role through its ability for an easier change to higher oxidation states than Ni ions, which reflects in a more favorable energetics of NiOOH formation and an improved urea oxidation reaction catalysis based on circular earth-abundant elements.

1. Introduction

The growing global demand for clean and sustainable energy has intensified research into hydrogen (H_2) as a high-energy, carbon-free fuel.[1] Electrochemical water splitting is widely regarded as a promising technology for H_2 generation, as it directly converts electrical energy, preferably from renewable sources, into chemical energy stored in molecular hydrogen.[2] However, the overall water-splitting process is kinetically hindered by the sluggish oxygen evolution reaction (OER) at the anode, which requires a high overpotential (typically >1.6 V vs. RHE) due to the complex four-electron transfer mechanism.[3] This kinetic bottleneck significantly reduces the overall energy efficiency of electrolytic hydrogen production and increases operational costs.[4]

In recent years, urea electrolysis has emerged as an attractive alternative anodic process to replace OER.[5,6] The urea electrooxidation reaction (UOR) (Equation (1)) possesses a much lower thermodynamic potential (0.37 V vs. RHE) than OER (1.23 V vs. RHE), offering the possibility to substantially reduce the overall cell voltage for hydrogen generation.[7–9] By coupling the hydrogen evolution reaction (HER) at the cathode with UOR at the anode, the total energy input can be decreased by up to 30–40%, thus improving the economic viability of electrochemical hydrogen production.[4,6]

$$6OH^- + (NH_2)_2\,CO \rightarrow 5H_2O + N_2 + CO_2 + 6e^- \quad (1)$$

Beyond energy efficiency, urea electrolysis provides an additional environmental benefit. Urea is a major constituent of various waste streams, particularly from agricultural runoff and municipal wastewater. The oxidative decomposition of urea not only generates hydrogen but also contributes to wastewater remediation by removing nitrogenous pollutants that can cause eutrophication.[10,11]

F. Bano, S. Zambonin, Prof. M. Roverso, Prof. L. Calvillo
Dipartimento di Scienze Chimiche, Università di Padova, Via Marzolo 1, 35131, Padova, Italy
E-mail: laura.calvillolamana@unipd.it
Dr. D. Chen, Dr. D. Perilli, Prof. C. Di Valentin
Department of Materials Science, Università degli Studi di Milano-Bicocca, Via Cozzi 55, 20125, Milan, Italy
E-mail: cristiana.divalentin@unimib.it
Dr. D. Mosconi
Circular Materials s.r.l, Via Bragni, 93F, 35010, Cadoneghe, Padua, Italy
Dr. V. Celorrio
Diamond Light Source Ltd, Diamond House, Harwell Science and Innovation Campus, Didcot, Oxfordshire OX11 0DE, UK
Prof. L. Calvillo
INSTM Research Unit, Via Marzolo 1, 35131, Padova, Italy
The ORCID identification number(s) for the author(s) of this article can be found under https://doi.org/10.1002/eem2.70465.

DOI: 10.1002/eem2.70465

Therefore, integrating urea electrolysis into wastewater treatment systems could simultaneously address both energy and environmental challenges, advancing the goals of sustainable development.

Despite these advantages, the practical implementation of UOR remains challenging. The reaction involves multiple proton-coupled electron transfer steps, leading to the formation of intermediates such as *CO, $*NH_2$, and *NCO, which can poison the catalyst surface and hinder reaction kinetics.[12] As a result, the design of highly active, selective, and stable electrocatalysts for UOR is a central focus of current research. Transition metal-based materials (TMs), including Ni, Co, and Fe oxides, hydroxides, and phosphides, have demonstrated promising activity in alkaline media due to their favorable adsorption energies for urea and intermediates.[8,12–15] Among all TMs, Ni-based materials are the most effective non-precious catalysts for UOR in alkaline conditions, although the measured onset potentials (about +1.4–1.5 V) are still far above the theoretical value (+0.37 V) due to the slow kinetics of CO_2 release.[16] Ni has limited availability and is also a water contaminant, but, interestingly, it can be removed from wastewater in the form of solid $Ni(OH)_2$, which is the best cost-effective reported UOR catalyst.[17] Recently, we have demonstrated that recovered Ni from electroless nickel plating wastewater in the form of solid $Ni(OH)_2$ can be used as efficient UOR catalysts in hybrid anion exchange membrane water electrolyzers.[18] In addition, the life cycle assessment (LCA) confirms that coupling urea oxidation with recycled nickel catalysts significantly lowers the CO_2-equivalent footprint of hydrogen production, demonstrating the effectiveness of this circular and energy-efficient approach.

However, the activity of this recovered Ni-based UOR catalyst could be improved to decrease the onset potential, which is still far above the theoretical value. Among the strategies to improve catalysts' activity, doping is a highly effective strategy to enhance the activity, stability, and kinetics of Nickel-based UOR electrocatalysts by regulating their electronic structure, promoting active phase reconstruction, and increasing the number of active sites.[19–22] In addition, this strategy can be easily incorporated during the Ni recovery process.

However, optimizing catalyst structures to suppress side reactions and improve long-term stability and understanding the detailed reaction mechanisms remain critical scientific and engineering challenges.[23]Experimental studies have proposed various mechanistic pathways, including both direct and indirect routes towards N_2 formation, but a unified mechanistic picture is still lacking.[16,17,24,25]

Density functional theory (DFT) has become an indispensable tool for probing the atomic-scale mechanisms of UOR and guiding catalyst design. DFT calculations provide insights into adsorption energies, reaction barriers, and the thermodynamics of intermediate species, which are often inaccessible through experiments alone. Theoretical studies on UOR have predicted different mechanisms (see Table S1, Supporting Information, for a summary of the existing works). Some confusion is related to the use of different β-NiOOH phases (e.g., L and S) or surface models. For instance, Daramola et al. proposed that the CO_2 desorption is the rate-determining step for NiOOH using a very simplified molecular model and the B3LYP functional, while Zhang et al., based on PBE + U + D3 calculations and (100) NiOOH surface, suggested that the oxidation of $*NH_2$ to *NH or the N_2 desorption determines the overall rate for NiOOH or NiOO surfaces, respectively.[26,27] Subsequent studies found a similar UOR mechanism for NiOOH (0001) surface but with a different N-H bond breaking potential-determining step (PDS). For example, Zheng et al. suggested that the PDS is the fourth dehydrogenation step from $*CON_2H$ to $*CON_2$ based on PBE + U calculations on (0001) surface of S phase of NiOOH while Jin et al. proposed that the PDS is the second dehydrogenation step from $*CON_2H_3$ to $*CON_2H_2$ according to their PBE + U + D3 calculations on (0001) surface of U phase of NiOOH and Mn doping slightly increases this overpotential.[28,29] Qin et al. found that the formation of O vacancies induced by vanadium doping shifts the rate-determining step of the UOR from *COOH deprotonation to the oxidation of $*NH_2$ to *NH.[30] Chen et al. suggested that the PDS is the fourth dehydrogenation step from $*CON_2H$ to $*CON_2$ based on PBE + D3 calculations on (0001) surface of S phase of Mo-doped NiOOH with the presence of O vacancies.[31] Therefore, the actual UOR mechanism is still under debate and might depend on the transition metal doping.

In this context, aiming at enhancing the performance of the Ni-based catalysts from circular nickel reported in our previous work,[18] we have performed a fundamental and systematic study about the effect of manganese doping, an environmentally friendly element. We have prepared nickel hydroxide samples without and with different Mn doping content by the same method used for the recovery of Ni from wastewater in collaboration with Circular Materials s.r.l.[32] For this study, we employed a synthetic Ni precursor, which allowed for better control over the final composition and enabled a more systematic investigation of Mn doping, since we confirmed that the electrochemical performance of synthetic and recovered $Ni(OH)_2$ were comparable. These materials have been characterized by combining experimental techniques with theoretical calculations (Grimme-corrected hybrid functional HSE06-D3) to achieve a highly accurate structural and electronic description of the materials under investigation, given the known limitations of DFT + U approach for this system.[33–36] Materials with different degree of Mn doping have been tested as UOR catalysts in comparison with the undoped system. Theoretical and experimental studies have also been combined to determine the role of Mn in the enhancement of the UOR activity and elucidate the mechanistic pathways of UOR. In this way, we aim to study the underlying mechanism and provide insights at the electronic and molecular levels for the rational design of sustainable, efficient, and durable urea oxidation catalysts. Results have demonstrated that Mn ions incorporated into the nickel hydroxide structure cause an electronic effect on the Ni ions, facilitating the formation of NiOOH under catalytic conditions, which is the UOR active phase, but not changing the reaction mechanism with the overpotential significantly decreased.

2. Results and Discussion

2.1. Morphological and Structural Characterization

The morphology of the synthesized hydroxides was examined using scanning electron microscopy (SEM). As shown in **Figure 1**a,b, the undoped nickel hydroxide consists of particles with irregular shapes and a broad size distribution, ranging from hundreds of nanometers to several hundred micrometers. The incorporation of Mn into the precursor solution does not significantly alter the particle morphology or size distribution (Figure 1c–h). This wide distribution can be directly attributed to the chosen synthesis method, which yields large amounts of material (~10 g) within a short reaction time (20 min). During this rapid synthesis, nucleation and growth occur almost simultaneously over a few minutes, resulting in particles of widely varying dimensions. The morphology of the synthetic materials resembles that of the recovered ones from wastewater using the same method.[18] Compared to

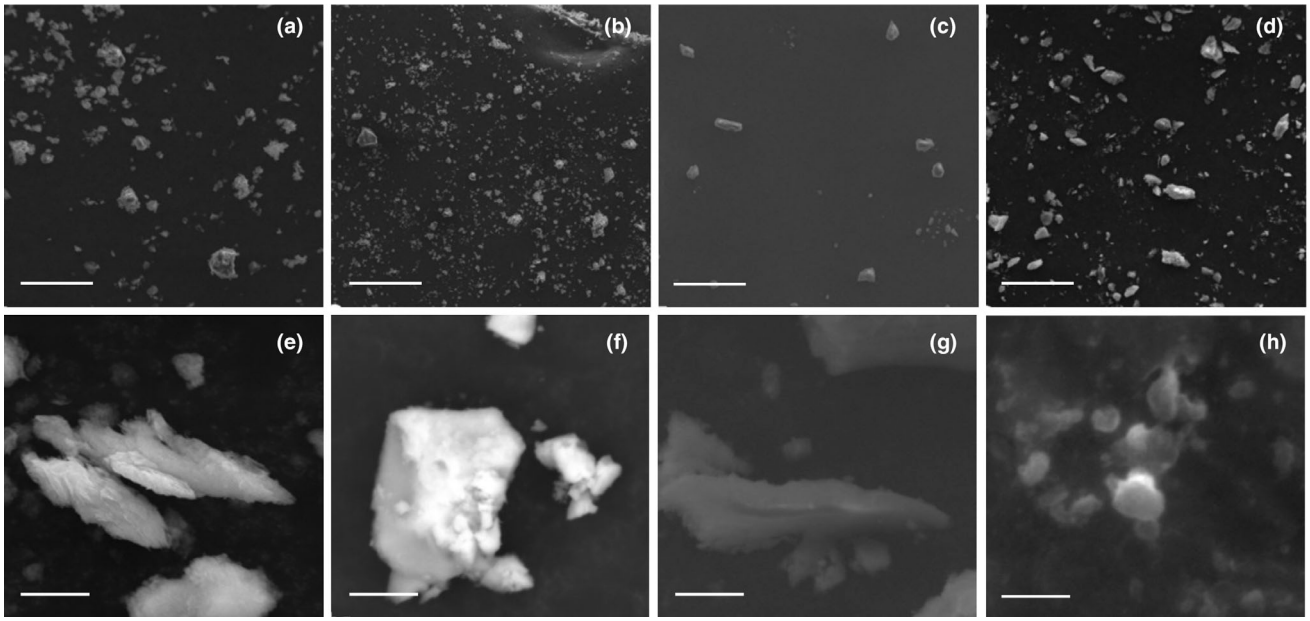

Figure 1. Representative SEM images of a, b) $Ni(OH)_2$; c, d) 3Mn-$Ni(OH)_2$; e, f) 5Mn-$Ni(OH)_2$; and g, h) 8Mn-$Ni(OH)_2$ samples at two different magnifications. The scale bar is 50 µm in (a–d) and 3 µm in (e–h).

more conventional approaches such as hydrothermal synthesis, our method is cost-effective, easily scalable for large-scale production, and suitable for generating substantial material quantities. However, it does not offer precise control over particle size and morphology.[37,38]

To assess the effectiveness of metal doping, energy-dispersive X-ray spectroscopy (EDS) and inductively coupled plasma mass spectrometry (ICP-MS) were performed. Table S2, Supporting Information, presents the atomic composition and Mn:Ni ratios obtained from both techniques. The results indicate that the atomic Mn:Ni ratios closely match the nominal values in all samples, confirming that our synthesis approach allows for reliable control over material composition.

The structure of the nickel hydroxide and the possible presence of secondary phases were investigated by X-ray diffraction (XRD) (**Figure 2a**). The XRD pattern of the undoped sample exhibits diffraction peaks at 19.3°, 33.1°, 38.6°, 59.1°, 62.8°, 69.4°, and 70.4°, corresponding to the (001), (100), (101), (110), (111), (200), and (103) planes, respectively, which are characteristic of the β-$Ni(OH)_2$ polymorph.[39] Additionally, a peak at 53.1°, assigned to the (210) plane of the α-$Ni(OH)_2$ polymorph, indicates the coexistence of both α- and β-phases, with β-$Ni(OH)_2$ being predominant.[39–41] This coexistence is commonly observed and is attributed to the lamellar structure of the material, which allows intercalation of water molecules within the *ab*-plane. Variations in the degree of hydration across the structure can lead to an interstratification phenomenon, in which both polymorphs coexist at the nanoscale.[39] The XRD patterns of the Mn-doped samples show the same set of reflections as the undoped sample, with no additional peaks corresponding to segregated Mn phases. This confirms that manganese is successfully incorporated into the $Ni(OH)_2$ structure. Further evidence of Mn incorporation is provided by a systematic shift of the diffraction peaks to higher angles with the Mn amount (Figure 2b), which is consistent with the substitution of nickel ions (Ni^{2+}, 0.69 Å) by manganese ions (Mn^{3+}, 0.645 Å), inducing a contraction of the crystal lattice that becomes more pronounced when increasing the Mn content.[42,43] In addition to this ionic-size effect, two further contributions likely reinforce the lattice contraction. First, Mn^{3+}–O bonds are expected to be more covalent than Ni^{2+}–O bonds because of the higher formal charge of Mn^{3+} (deduced from XAS analysis, see below), which increases the polarization of the metal–oxygen bond. It should be noted that the incidence of the bond covalency can be relevant enough to completely subvert the expected trend based on ionic radii alone.[44] Second, the Jahn–Teller activity of high-spin Mn^{3+} introduces local distortions of the octahedra. In our case, however, the XRD peak shift indicates that the overall contraction of the average structure is the dominant effect, while Jahn–Teller distortions remain a more local perturbation.

The diffraction peaks of the Mn-doped samples also exhibit reduced intensity compared with the undoped nickel hydroxide, indicating lower crystallinity.[45] Moreover, the (100) reflection broadens progressively with increasing Mn content (Figure 2b), suggesting a reduction in crystallite size upon doping.[42] This trend is quantitatively supported by the crystallite sizes calculated using the Scherrer equation, reported in Table S3, Supporting Information. As anticipated, the crystallite size decreases from 10.4 nm for the undoped sample to 4.8 nm for the sample with the highest Mn content.

To gain further insight into the nickel hydroxide structure and the oxidation states of Ni and Mn ions, X-ray absorption spectroscopy (XAS) was performed on the undoped sample and the one with the highest Mn content. Figure 2c,d show the X-ray Absorption Near Edge Structure (XANES) and the corresponding phase uncorrected Fourier-transformed Extended X-ray Absorption Fine Structure (FT-EXAFS) spectra at the Ni K-edge for both samples. The Ni K-edge XAS spectra of the $Ni(OH)_2$ and 8Mn-$Ni(OH)_2$ samples closely resemble that of the $Ni(OH)_2$ reference standard, confirming that the local structure remains consistent and that nickel is present in the +2 oxidation state, as expected. The main difference observed in the XANES region upon Mn doping is an increase in the intensity of the white line (peak

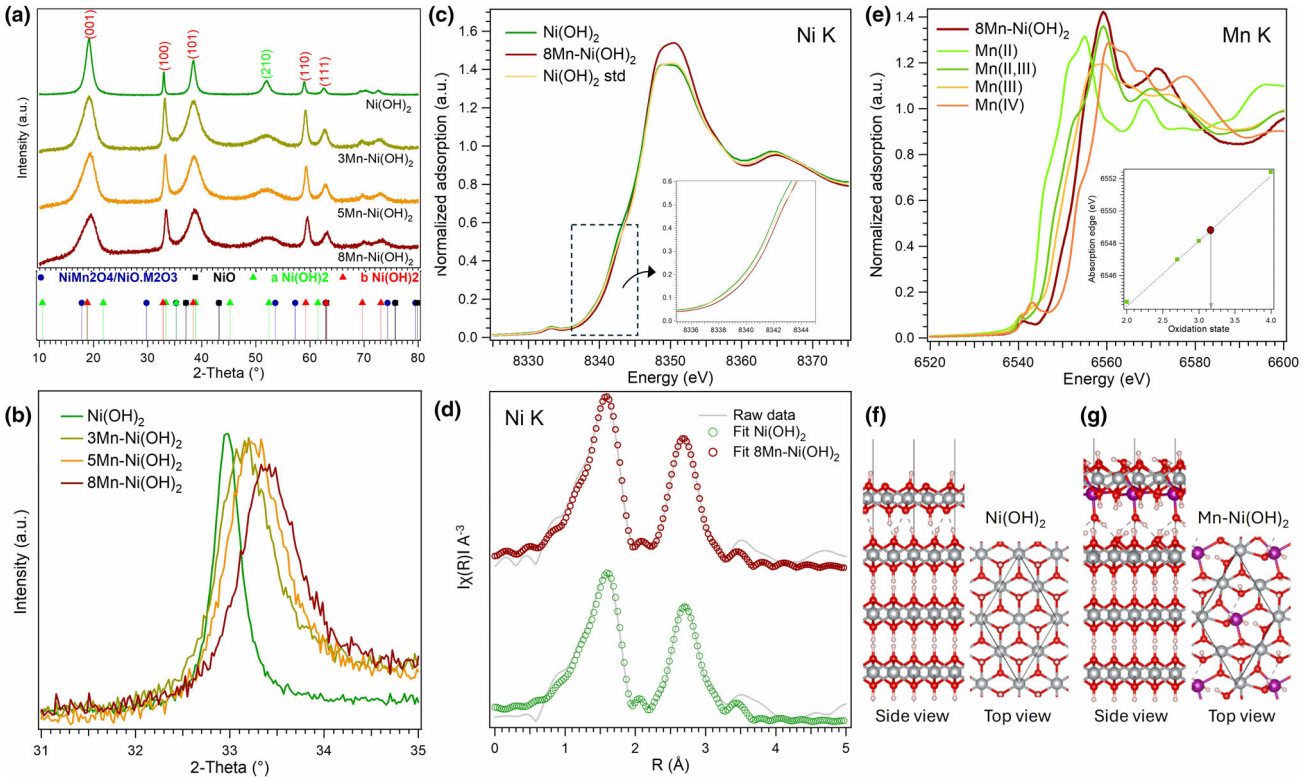

Figure 2. a) XRD patterns of the nickel hydroxide–based samples; b) detail of the (100) diffraction peak; c) XANES, and corresponding d) FT-EXAFS spectra at the Ni K-edge for the $Ni(OH)_2$ and 8Mn-$Ni(OH)_2$ samples; e) XANES region at the Mn K-edge for 8Mn-$Ni(OH)_2$; and f, g) side and top view of (0001) facet of the four-layer slabs of β-$Ni(OH)_2$, without (f) and with 25% Mn doping in the top layer (6.25% for the unit cell; in the Mn-doped model 1 OH was added to have charge balance due to the 3+ charge of the Mn ion) (g). XRD patterns in (a) are normalized with respect to the (001) peak intensity. The references used for the determination of the Ni and Mn oxidation state are also shown in (c) and (e). The inset in (c) is the detail of the absorption edge, while the one in (e) shows the determination of the oxidation state of Mn. In (f) and (g), the gray, purple, red, and pink balls represent Ni, Mn, O, and H atoms, respectively.

around 8350 eV). This enhancement indicates a perturbation of the electronic structure of Ni due to Mn incorporation, specifically reflecting a higher number of unoccupied Ni 3d states.[43,46] Mn incorporation modifies the local electronic structure through differences in electronegativity and preferred coordination chemistry between Mn and Ni. This affects the degree of Ni–O–M (M=Ni, Mn) hybridization, leading to a redistribution of electron density within the metal–oxygen network.[47] As a consequence, Ni sites become more electron-deficient, which is directly reflected in the increased white line intensity. This effect is also observed in the slight shift of the absorption edge of the 8Mn-$Ni(OH)_2$ sample, which suggests the formation of some Ni^{3+}-like sites, as already reported in the literature.[46,48]

The FT-EXAFS spectra of the $Ni(OH)_2$-based samples display a prominent peak at ∼1.6 Å, corresponding to Ni–O interactions, and another one at ∼2.76 Å, attributed to Ni–Ni or Ni–Mn coordination.[43,46] In the Mn-doped sample, the second peak slightly shifts to a lower radial distance (2.73 Å) (Figure S1, Supporting Information), which is consistent with the lattice contraction observed in the XRD analysis.[49] This trend is also supported by the bond distances obtained from the EXAFS fit and by literature reports showing that Ni–O and Ni–M bond lengths shorten upon Mn doping.[46] The parameters obtained from the fit are summarized in Table S4, Supporting Information, while the fit is included in Figure 2d. As anticipated, the Ni–O and Ni–M bond lengths tend to shorten when Mn^{3+} substitutes Ni^{2+}, being 2.061 and 3.106 Å, respectively, in the 8Mn-$Ni(OH)_2$ sample with respect to 2.066 and 3.126 Å in $Ni(OH)_2$. This result is consistent with the analysis of XRD data presented above.

Analysis of the Mn K-edge XANES spectrum (Figure 2e) indicates an average oxidation state of +3.17 for Mn (see inset in Figure 2e), which indicates the presence of Mn^{3+} ions in the bulk structure of $Ni(OH)_2$. An oxidation state slightly higher than +3 can be attributed to the partial presence of Mn^{4+} species at the nanoparticle surface, formed via oxidation of Mn^{3+} upon air exposure (see XPS analysis below). Previous studies have shown that Mn^{3+} ions can substitute Ni^{2+} in the $Ni(OH)_2$ lattice, leading to an excess of positive charge in the hydroxide layers.[43,46] This charge imbalance is compensated by the intercalation of anions between the layers.[46] The Mn K-edge FT-EXAFS spectrum (Figure S1, Supporting Information) exhibits a peak at ∼1.44 Å, corresponding to Mn–O interactions, and a second peak at ∼2.79 Å, associated with Mn-Ni/Mn coordination.[46]

The experimental results obtained for the undoped and Mn-doped nickel hydroxides were combined with density functional theory (DFT) calculations to confirm that +3 is the most stable oxidation state of Mn in the $Ni(OH)_2$ structure. The atomic structure of the (0001) surface of β-$Ni(OH)_2$ without/with 6.25% Mn doping for the unit cell was modeled using four-layer slabs with 4 M (M=Ni and Mn) atoms per

layer. The atomic positions of the two topmost layers were optimized, with the optimized structures shown in Figure 2f,g. Based on our calculations, Mn exhibits a +3 valence state in Mn-doped β-$Ni(OH)_2$, in line with the XAS results. The presence of Mn^{3+} in β-$Ni(OH)_2$, which has a higher oxidation state than Ni^{2+}, is compensated by the intercalation of OH^- species into the interlayers of Mn-doped β-$Ni(OH)_2$ (between the top and second layers) to maintain charge neutrality, consistent with experimental observations that Ni atoms are in a +2 valence state for both undoped and Mn-doped $Ni(OH)_2$. Comparison of the optimized structures of the undoped (Figure 2f) and Mn-doped (Figure 2g) systems reveals a pronounced distortion in the top layer of the Mn-doped case. This structural distortion originates from the combined effects of the altered charge distribution within the metal sublattice and the presence of the additional OH^- ligand.

The oxidation states of nickel and manganese at the nanoparticle surface were determined by X-ray photoelectron spectroscopy (XPS). Figure S2, Supporting Information, shows the Ni $2p_{3/2}$ and Mn 2p regions for both undoped and Mn-doped samples. All samples exhibit the same Ni 2p spectrum, which is characteristic of $Ni(OH)_2$.[50,51] To further confirm the exclusive presence of $Ni(OH)_2$, the Ni 2p spectrum was deconvoluted using seven components corresponding to various features associated with nickel hydroxide, such as peak asymmetry, multiplet splitting, shake-up satellites, and plasmon loss structures (Figure S2a, Supporting Information).[45,50,51] A good fit was achieved using only these components, confirming the absence of other nickel-containing phases, in agreement with the XRD results. Consequently, no additional components were included in the analysis. The Mn 2p region is presented in Figure S2b, Supporting Information. As expected, the intensity of the Mn signal increases with higher doping levels. However, it is important to note that the Ni $L_2M_{23}M_{45}$ Auger peak overlaps with the Mn 2p region, which can compromise the accuracy of the analysis, especially at lower Mn concentrations.[52] Therefore, only the spectrum of the sample with the highest Mn content was analyzed in detail. This analysis reveals the presence of Mn^{4+} at the surface of the particles, consistent with the oxidation of Mn^{3+} upon exposure to air, and in agreement with previous works.[46] This finding supports the XANES results, which also indicate the presence of a small fraction of Mn^{4+}. The high Mn^{3+}/Mn^{4+} ratio observed in the material can be explained by considering the material's morphology. The particle size obtained through our synthesis method is relatively large, often reaching several microns. As a result, the ratio of bulk to surface Mn is high, which agrees with the observed Mn^{3+}/Mn^{4+} ratio.

The Mn:Ni surface ratio of the nanoparticles was determined by analyzing the Ni 2p and Mn 2p regions and applying the corresponding sensitivity factors. The results, summarized in Table S2, Supporting Information, are in close agreement with the nominal ratio as well as with values obtained from ICP-MS and EDX analyses. This consistency suggests a homogeneous distribution of Mn throughout both the bulk and the surface of the material, effectively ruling out any metal segregation.

2.2. Electrochemical Characterization and Mechanistic Studies

Initially, the samples were tested in the absence of urea to determine the electrochemical surface area (ECSA), used to normalize the current and determine the catalysts' intrinsic activity, and to investigate any potential effect of Mn on the Ni^{2+}/Ni^{3+} redox potential. **Figure 3**a presents the cyclic voltammograms (CVs) recorded without urea for all

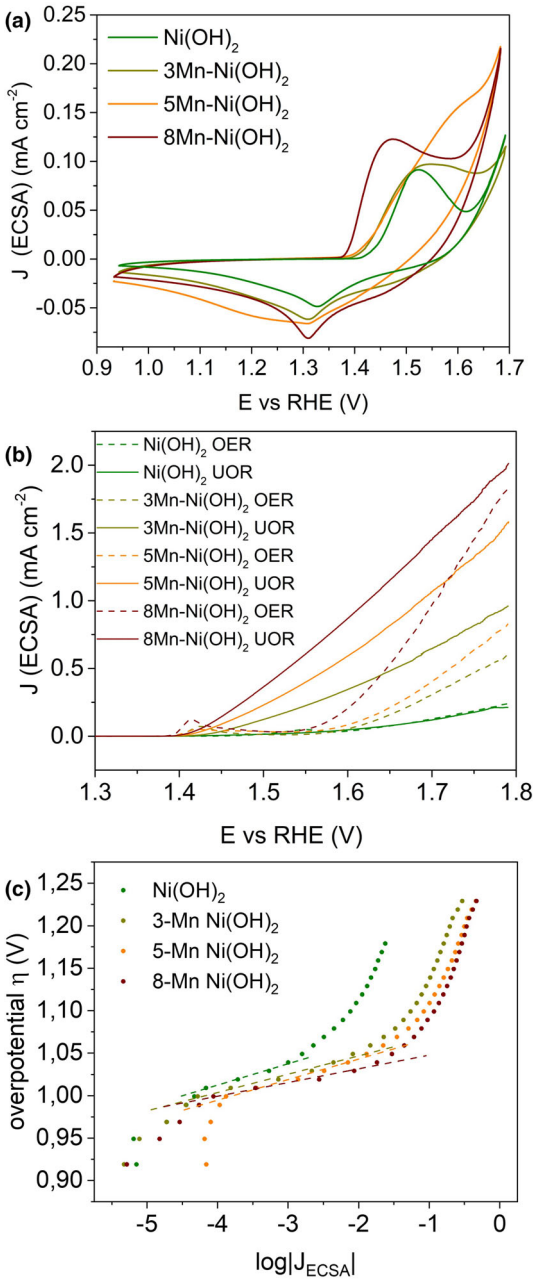

Figure 3. a) CVs in N_2-saturated 1 M KOH; b) LSVs in N_2-saturated 1 M KOH and 1 M KOH + 0.33 M Urea; and c) Tafel analysis for all the nickel hydroxide–based catalysts. Current in (a) and (b) is normalized by ECSA.

samples. The ECSA values, calculated from the Ni^{2+}/Ni^{3+} reduction peak, are reported in Table S5, Supporting Information.

In the CVs shown in Figure 3a, an oxidation peak between 1.4 V and 1.5 V, corresponding to the oxidation of Ni^{2+} to Ni^{3+}, and the associated reduction peak at approximately 1.3 V are observed for all samples.[53] The oxidation of Ni^{2+} in $Ni(OH)_2$ leads to the formation of the NiOOH phase, which is widely recognized as the active species in UOR.[54] A gradual shift of the Ni^{2+}/Ni^{3+} oxidation peak towards lower potentials is observed with increasing Mn content, indicating that Mn facilitates the oxidation of Ni species. This behavior is attributed to

an electronic effect induced by Mn^{3+} on Ni^{2+}, as also suggested by XANES analysis. To support this hypothesis, we calculated the energy required for the Ni^{2+} to Ni^{3+} oxidation (β-$Ni(OH)_2 \rightarrow \beta$-NiOOH), with results reported in Table S6, Supporting Information. In addition, the model of NiOOH, with and without Mn, is also described in the Figure S3, Supporting Information. The calculations show that Mn doping significantly lowers the oxidation energy from 9.9 eV to 9.1 eV, a reduction of approximately 8%, which aligns well with the experimental observation of the redox peak shift to lower potentials upon Mn incorporation.

Figure 3b displays the linear sweep voltammograms (LSVs) recorded within the potential window relevant to the UOR in the absence and presence of urea. In the absence of urea, the oxidation current observed at potentials above 1.6 V is attributed to the oxygen evolution reaction (OER). A moderate improvement in OER activity is observed upon Mn doping. All Mn-containing samples exhibit better performance compared with the undoped $Ni(OH)_2$, as evidenced by increased current densities and a shift of the onset potential towards lower values with increasing Mn content. A detailed study of the effects of Mn doping on the OER activity is reported in our work, currently under revision.[55]

In the presence of urea, a significant shift in the onset potential—up to 150 mV for the 8Mn-$Ni(OH)_2$ sample—is observed in Mn-doped materials compared to their OER onset (absence of urea). This shift aligns with the onset of the Ni^{2+}/Ni^{3+} redox peak, confirming that Ni^{3+} species, in the form of NiOOH, act as the catalytically active sites during UOR. Furthermore, Mn-containing samples reach higher current densities in the presence of urea, reinforcing the role of Mn in enhancing catalytic activity via its electronic influence on Ni. Accordingly, an increase in UOR performance is observed with increasing Mn content. This trend is consistent with previous reports in the literature, where Mn incorporation led to an onset potential shift of approximately 40 mV.[56,57] By contrast, in the present study, the shift increases with Mn content, reaching up to 150 mV for the 8Mn-$Ni(OH)_2$ sample. Tafel slopes for UOR were determined and are reported in Figure 3c and Figure S4, Supporting Information. Values obtained are very similar for all the samples ($\sim$30 mV dec^{-1}) and agree with the ones reported in the literature.[8] The similarity of these values implies a similar reaction mechanism with the same rate-determining step (RDS) for all the samples. Only the sample with the highest amount of Mn shows a slightly lower Tafel slope (18 mV dec^{-1}) than the other materials, suggesting fast charge transfer and more favorable kinetics thanks to the Mn effect. Electrochemical impedance spectroscopy (EIS) measurements under UOR conditions confirmed the lower charge transfer resistance in 8Mn-$Ni(OH)_2$ than in $Ni(OH)_2$ (Figure S5, Supporting Information). Unfortunately, to the best of our knowledge, theoretical Tafel slope values have not been reported and assigned to specific elementary steps yet for UOR. Therefore, we cannot relate our Tafel slope values to specific UOR elementary steps.

To address this gap and correlate the experimentally obtained Tafel slopes with the PDS, we investigated the reaction under alkaline conditions using DFT calculations, thus gaining deeper insights into the UOR mechanism and the role of Mn incorporation. The pathway considered involves the oxygen vacancy site of β-NiOOH as the active center, following previous studies reported in the literature (see Table S1, Supporting Information).[12,58] Additionally, experimental evidence confirms that N_2 production is governed by an intramolecular mechanism rather than intermolecular N–N bond coupling.[25] Based on this, we propose the UOR pathway illustrated in **Figure 4** and summarized in Table 1. As shown in Figure 4a, the $CONH_2NH_2$ molecule initially dissociatively adsorbs onto the oxygen vacancy site of NiOOH surface by filling it with the carbonyl O atom, with a favorable reaction free energy of approximately −1.97 eV (Step 1, Table 1). During structural optimization, one proton from one NH_2 is spontaneously transferred to the surface and binds to a nearby oxygen atom, stabilizing the system without the formation of radical species (*$CONH_2NH\_H$). Subsequently, the adsorbed intermediate undergoes a sequence of deprotonation and dehydration steps, transitioning through the *$CONH_2NH$, *$CONH_2N$, *CONHN, and *CONN intermediates. Among these, the fourth dehydrogenation step (*CONHN → *CONN) is the most endergonic, with an energy increase of 2.26 eV, and is identified as the PDS (Step 5, Figure 4 and Table 1). This finding aligns with experimental observations indicating that N–N bond formation (Step 7, Figure 4) is not the rate-limiting.[25] Indeed the N–N bond is formed in the next step going from *CONN to *CON_2. The N_2 release leaves a physisorbed *OC which, after atomic rearrangement, becomes chemically adsorbed as *CO. An OH^- ion is then oxidized and binds to the *CO intermediate to form *COOH. Finally, the *COOH species undergoes deprotonation to produce H_2O and CO_2, releasing a significant amount of energy. This exoergonic step is likely associated with CO_2 formation, given to the large energy consumption for the deprotonation and dehydration during steps 2–5.

After analyzing the UOR mechanism in the undoped system, we then focused on the case of the Mn-doped system. Specifically, we investigated the UOR mechanism on the Mn-doped NiOOH (0001) surface, with a doping concentration of 6.25% Mn per unit cell. We put Mn in different configurations (Figure S6, Supporting Information). When it is in the Mn1 configuration, we register the lowest oxygen vacancy formation energy, as detailed in the SI (Table S7, Supporting Information). The reaction pathway for this Mn-doped system, illustrated in Figure 4b and summarized in Table 1, reveals a notable reduction in overpotential, from 1.89 V in the undoped case (calculated as 2.26–0.37 V, where 0.37 V corresponds to the minimum thermodynamic potential required for UOR) to 1.50 V upon Mn doping. Step 5 (*CONHN → *CONN) remains the PDS, as for the undoped system, in good agreement with experimental results that indicate that the presence of Mn dopants does not change the RDS. This computational result confirms that Mn doping significantly enhances the UOR activity of NiOOH by decreasing the overpotential but without altering the rate-limiting step. Considering the experimental Tafel slope values obtained for the undoped and doped samples, we can assume that values between 18 and 30 mV dec^{-1} are associated with the fourth dehydrogenation step (*CONHN → *CONN) as RDS.

We have analyzed the oxidation states on the metal atoms in the top layer for intermediates *CONHN and *CONN and found that, while two Ni ions (out of four in the top layer) are oxidized to Ni^{3+} in the undoped catalyst, all Ni ions are +2 with the Mn ion being +4 in the Mn-doped catalyst (see Table S8, Supporting Information). This situation favors the stability of these intermediates in the doped case with respect to the undoped one, but the effect is larger for *CONN that explains the reduction in the overpotential. Furthermore, we observe that Mn doping strongly promotes the adsorption of the urea molecule, as recently reported in the literature.[29] The reaction free energy for Step 1 increases from −1.97 eV in the undoped β-NiOOH-U system to −2.94 eV in the Mn-doped case, further contributing to the improved UOR performance.

Although the cost to form the O vacancy is higher, we also investigated the catalytic activity for the other three Mn doping sites since it could potentially be superior. On the contrary, we found that the

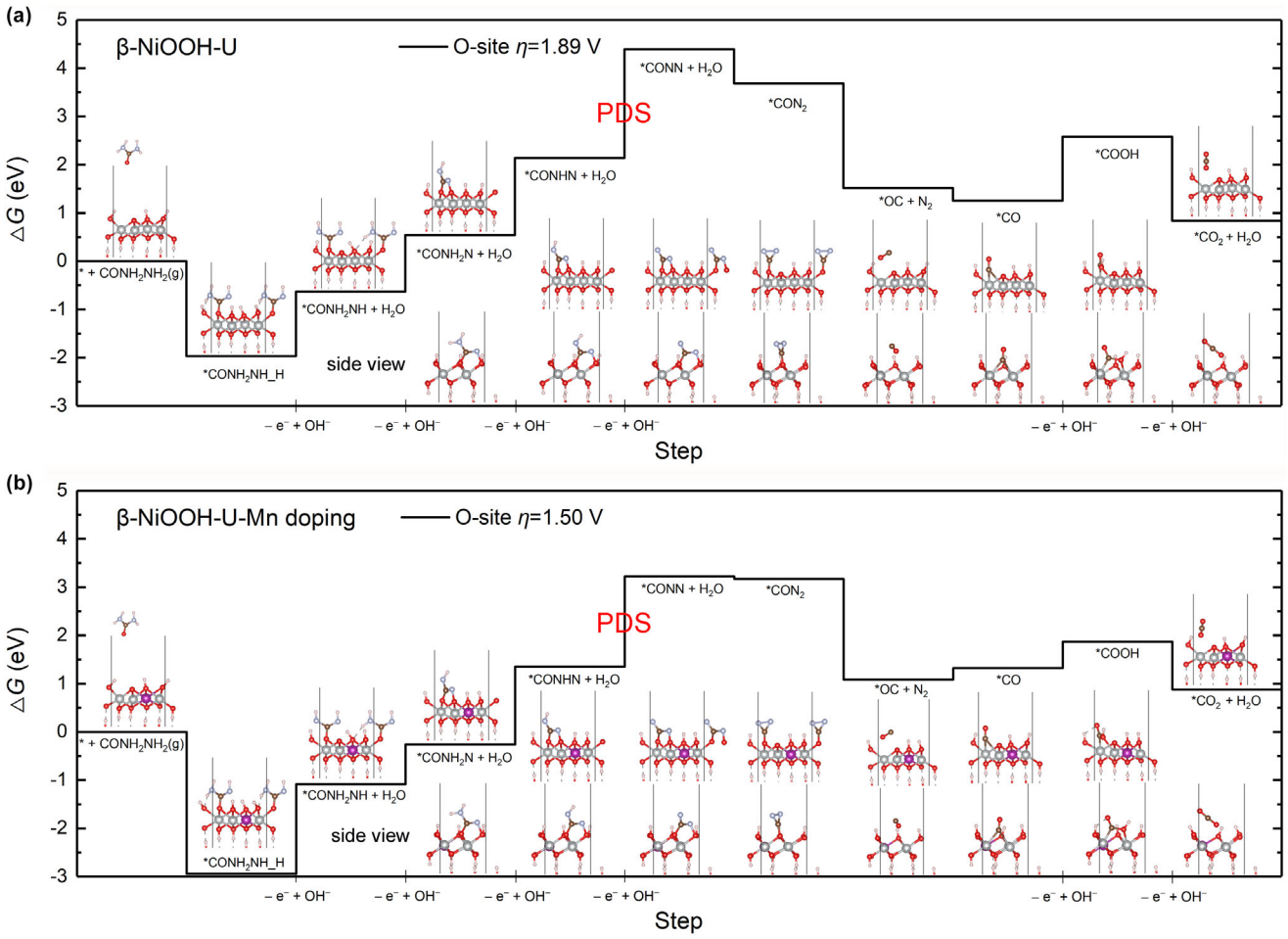

Figure 4. UOR free energy profile calculated using the HSE06 + D3 method on a four-layer slab model: a, b) β-NiOOH-U (0001) surface without/with Mn1 doping (6.25% for the unit cell). The main view of the atomic structure of intermediates is illustrated inside the Figure. The side views of *$CONH_2N$, *CONHN, *CONN, *CON_2, *OC, *CO, *COOH, and *CO_2 are also shown for clarity. The electrochemical steps are identified at the x-axis by indicating ($-e^- + OH^-$).

overpotential is not as low as for Mn1 (see Table S9 and Figure S7, Supporting Information).

Since XRD analysis revealed that the sample consists of a mixture of α- and β-$Ni(OH)_2$, with the β-phase being predominant (Figure 2a), we extended our mechanistic investigation to the γ-NiOOH phase. This phase originates from the electrochemical oxidation of α-$Ni(OH)_2$, and the corresponding results are provided in the ESI (Table S10, Supporting Information). As shown in Figure S8, Supporting Information, Mn1-doped γ-NiOOH displays an UOR overpotential comparable to that of Mn1-doped β-NiOOH-U, without affecting the rate-limiting step. These results indicate that the initial $Ni(OH)_2$ phase does not affect the UOR mechanism.

2.3. Products' Analysis

As a proof of concept, rotating ring-disk electrode (RRDE) measurements were conducted to determine whether the observed current density originated from UOR or from the competing OER.[59] **Figure 5**a shows the results for the 8Mn-$Ni(OH)_2$ sample as a representative case, while data for the remaining samples are presented in Figure S9, Supporting Information. In 1 M KOH (without urea), a reduction current is detected at the Pt ring simultaneously with the oxidation current at the disk, indicating the reduction of oxygen generated during OER at the disk surface. By contrast, when the experiment is performed in the presence of urea, no current is detected at the ring up to 1.7 V. This key observation confirms that oxygen evolution does not occur under these conditions. Therefore, the oxidation currents recorded at the disk are exclusively attributed to UOR. These results further highlight the high selectivity of the $Ni(OH)_2$-based samples towards UOR within this potential range. A slight change in the slope of the UOR LSV curve is observed around 1.7 V, suggesting a possible shift in mechanism or selectivity. Indeed, at potentials above 1.7 V, a small reduction current appears at the ring, confirming that OER begins to dominate at higher potentials. Notably, these results are in good agreement with those obtained for $Ni(OH)_2$ recovered from wastewater. In our previous work, during differential electrochemical mass spectrometry (DEMS) studies, we already observed that the presence of urea induces a shift

Table 1. Reaction free energies of the 10 steps of the UOR at the O site of β-NiOOH-U (0001) facet without/with Mn doping (6.25% for the unit cell) calculated using the HSE06 + D3 method.

System	Step	Equation	Reaction free energy (eV)
β-NiOOH-U	1	$* + CONH_2NH_2(g) \rightarrow *CONH_2NH\_H$	−1.97
	2	$*CONH_2NH\_H + OH^- \rightarrow *CONH_2NH + H_2O + e^-$	1.33
	3	$*CONH_2NH + OH^- \rightarrow *CONH_2N + H_2O + e^-$	1.17
	4	$*CONH_2N + OH^- \rightarrow *CONHN + H_2O + e^-$	1.60
	5	$*CONHN + OH^- \rightarrow *CONN + H_2O + e^-$	2.26 (η = 1.89)
	6	$*CONN \rightarrow *CON_2$	−0.71
	7	$*CON_2 \rightarrow *OC + N_2$	−2.16
	8	$*OC \rightarrow *CO$	−0.27
	9	$*CO + OH^- \rightarrow *COOH + e^-$	1.33
	10	$*COOH + OH^- \rightarrow *COO + H_2O + e^-$	−1.74
Mn1-doped β-NiOOH-U	1	$* + CONH_2NH_2(g) \rightarrow *CONH_2NH\_H$	−2.94
	2	$*CONH_2NH\_H + OH^- \rightarrow *CONH_2NH + H_2O + e^-$	1.86
	3	$*CONH_2NH + OH^- \rightarrow *CONH_2N + H_2O + e^-$	0.82
	4	$*CONH_2N + OH^- \rightarrow *CONHN + H_2O + e^-$	1.61
	5	$*CONHN + OH^- \rightarrow *CONN + H_2O + e^-$	1.87 (η = 1.50)
	6	$*CONN \rightarrow *CON_2$	−0.05
	7	$*CON_2 \rightarrow *OC + N_2$	−2.08
	8	$*OC \rightarrow *CO$	0.24
	9	$*CO + OH^- \rightarrow *COOH + e^-$	0.55
	10	$*COOH + OH^- \rightarrow *COO + H_2O + e^-$	−0.99

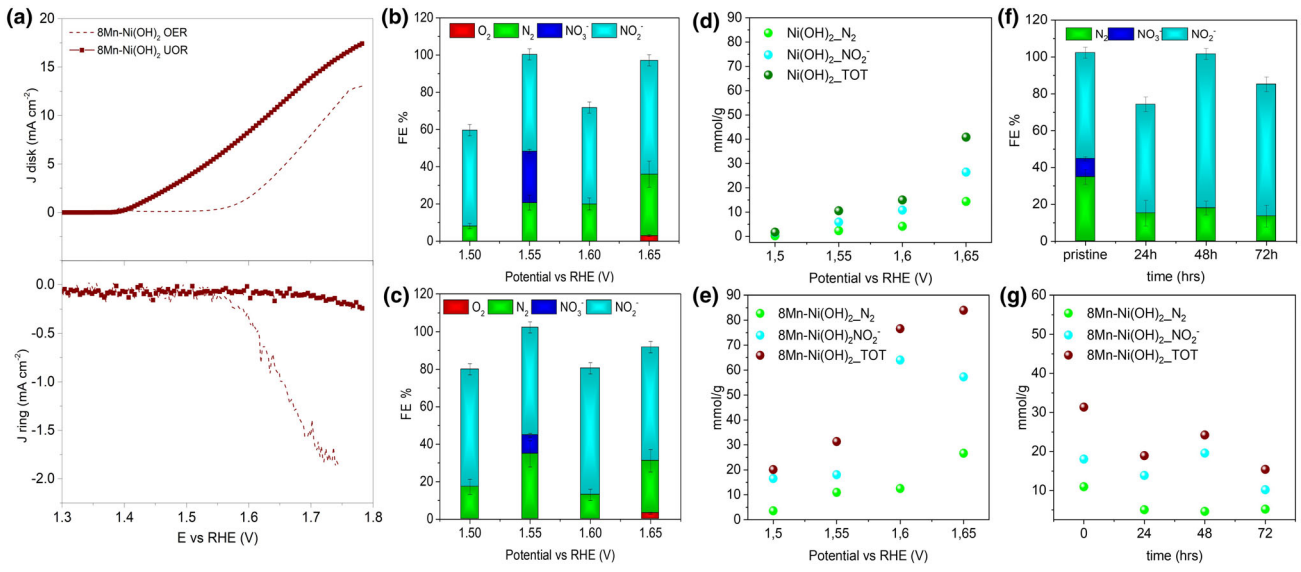

Figure 5. a) RRDE results for the 8Mn-Ni(OH)$_2$ sample; b–c) faradaic efficiency for UOR/OER products on Ni(OH)$_2$ (b) and 8Mn-Ni(OH)$_2$ (c); and d–e) corresponding quantification of N products (mmol g_{cat}^{-1}) on Ni(OH)$_2$ (d) and 8Mn-Ni(OH)$_2$ (e) at different applied potentials; and f) faradaic efficiency for UOR products on 8Mn-Ni(OH)$_2$; and g) corresponding quantification of N products (mmol g_{cat}^{-1}) as a function of time. Error bars in (b), (c), and (f) indicate the propagation of errors based on calibration curves.

towards more positive values of the OER onset potential, and that there is a 300–350 mV separation between the onset potentials of N_2 and O_2 evolution under UOR conditions.[18]

The determination and quantification of gaseous and liquid nitrogen-containing products derived from the UOR were conducted using gas chromatography and ion chromatography, respectively.

Under alkaline conditions, the expected UOR products are molecular nitrogen (N_2) and carbon dioxide (CO_2). However, it is well established that urea overoxidation can generate nitrite (NO_2^-), nitrate (NO_3^-), and cyanate (CNO^-) species, with NO_2^- typically being the predominant product.[8,13,59–61] Beyond being an intermediate in nitrogen-cycle chemistry, the generated nitrite ions can serve as valuable precursors for green chemical syntheses, including the production of nitrates, nitric oxide–releasing compounds, and other nitrogen-based functional materials, highlighting the potential dual utility of UOR systems in both energy conversion and chemical valorization.

The potential-dependent Faradaic efficiency (FE) for each ionic and gaseous product generated from UOR and/or OER on $Ni(OH)_2$ and 8Mn-$Ni(OH)_2$ electrodes is presented in Figure 5b,c. Carbon-containing products from UOR, such as cyanate (CNO^-) and carbon dioxide (CO_2), were not quantified; CO_2 was not detected in the gas phase, consistent with our previous analysis using a hybrid electrolyzer.[18] This absence is attributed to the high absorption capacity of the alkaline electrolyte, which promotes the formation of carbonate ions (CO_3^{2-}). Therefore, the reported FE values are based solely on nitrogen-containing species. Interestingly, $Ni(OH)_2$ recovered from wastewater, as investigated in our previous work, and $Ni(OH)_2$ synthesized from synthetic Ni precursors using the same synthesis method in the present study exhibit comparable electrochemical behavior and generate the same products during the UOR. This occurs despite the presence of impurities and multiple Ni phases in the recycled material.

Notably, both $Ni(OH)_2$ and 8Mn-$Ni(OH)_2$ exhibit very similar product distributions, with NO_2^- being the main product, in agreement with previous reports where it has been demonstrated that the overoxidation of urea to NO_2^- usually dominates over its oxidation to N_2 at Ni $(OH)_2$-based anodes.[8,13,18,59,61,62] However, it has also been stated that, in addition to the higher chemical value of nitrites than N_2 mentioned above, the coupling of the hydrogen evolution reaction with UOR to nitrites is more efficient than the coupling with UOR to N_2.[63,64]

The comparable product distributions observed for samples with and without Mn are consistent with the experimental and computational findings discussed above. Manganese does not act as an active site in the catalytic process and thus does not alter the intrinsic UOR reaction pathway or the products formed. Instead, Mn plays an electronic-modulation role, adjusting the electron density of the Ni active sites and thereby facilitating the $Ni(OH)_2$ to NiOOH transformation at lower applied potentials. This indirect effect of Mn on UOR is clearly illustrated in Figure 5d,e, which depict the number of product moles per catalyst mass at different applied potentials. In both catalysts, product generation increases with increasing potential, in line with the rise in current density. However, the total number of moles produced is substantially higher for the Mn-containing sample. For instance, at 1.6 V, the total amount of products generated by 8Mn-$Ni(OH)_2$ is approximately five times greater than that for $Ni(OH)_2$. Therefore, at a given potential, Mn doping enhances the overall urea oxidation rate, resulting in increased hydrogen evolution at the cathode.

To further evaluate catalyst's stability and the temporal evolution of activity and selectivity, 8Mn-$Ni(OH)_2$ was subjected to an aging protocol. Long-term chronoamperometric measurements were conducted to directly probe activity and selectivity as a function of time (Figure 5f, g). As shown in Figure 5f, N_2 and nitrite remain the dominant products, and the FEs exhibit no significant variation, confirming stable selectivity under continuous operation. A moderate decrease in production rate is observed after 24 h, which could be related to surface poisoning by reaction intermediates,[18] or partial detachment of the catalytic material. After this initial drop, however, the production rate stabilizes and enters a quasi-steady-state regime (Figure 5g). Therefore, we can conclude that our material has a high catalytic stability with time after a slight initial activity loss. To the best of our knowledge, stability tests of UOR catalysts for a so long time and studies about the variation of products with time have not been reported in the literature.

3. Conclusions

In this work, we synthesized manganese-doped nickel hydroxides by a synthesis route that mimics Ni recovery from wastewater and carefully characterized them by combining experimental and theoretical techniques. Thanks to this approach, we determined that Mn^{3+} incorporation modifies the $Ni(OH)_2$ structure, shortening the Ni–O and Ni–Ni/Mn bond distances, and modulates the energetics of several processes: 1) reduces the cost to oxidize the top layer of $Ni(OH)_2$ to NiOOH by 0.8 eV; 2) increases the adsorption free energy of urea (step 1) of 1 eV; 3) lowers the overpotential for UOR by 0.49 V. Mechanistic studies have shown that Mn dopants do not directly participate in the UOR reaction, and that the *CONHN → *CONN dehydrogenation is the PDS both when Mn is present and absent, confirming that Mn does not participate in the reaction mechanism. Our $Ni(OH)_2$-based catalysts are very selective towards UOR up to 1.7 V, while at higher potential UOR starts competing with OER. The main products obtained from UOR on the $Ni(OH)_2$-based materials are nitrogen and nitrites, and their production rate is very stable with time. The Mn incorporation does not change the products distribution but enhances the overall urea oxidation rate, resulting in a substantially higher number of product moles formed at a specific applied potential.

4. Experimental Section

Synthesis of Mn-doped $Ni(OH)_2$ powders: Nickel hydroxide samples with different Mn doping (0 at.%, 3 at.%, 5 at.%, 8 at.%) were prepared by Circular Materials S.r.l. following a patented method using manganese and nickel acetates (Mn $(CH_3COO)_2$, $Ni(CH_3COO)_2$, Sigma-Aldrich) as metal precursors and supercritical water as solvent.[32] The synthesis parameters are summarized in Table S12, Supporting Information. Briefly, the corresponding amount of $Mn(CH_3COO)_2$ was added to 0.5 L of a 0.3 M $Ni(CH_3COO)_2$ solution. Using the Circular Materials srl continuous flow pilot plant, the metal-containing solution was firstly pumped in the plant and mixed with a stream of 1 M NaOH to adjust the pH. Such obtained solution was then driven by pumps to the plant reactor, where the material precipitation occurs thanks to the mixing with a third stream of supercritical water (430 °C; 220 bar). The estimated residence time in the reactor is 1–2 s. Following the reaction step, the final stream is cooled down and depressurized. The relative flows of the streams can be individually tuned to set the experiment conditions, which for these materials were 270 °C (reactor temperature) and pH 13 at the plant output. Subsequently, the solution was centrifuged to obtain the final material that was dried in an oven at 105 °C overnight. Finally, the solid grains were grinded into a fine powder in a mortar. Samples were labeled as X Mn-$Ni(OH)_2$, where X refers to the atomic Mn doping that is equal to 3, 5, 8. For simplicity, the undoped sample was just labeled as $Ni(OH)_2$.

Physicochemical characterization: Scanning electron microscopy (SEM) images and energy-dispersive X-ray spectroscopy (EDS) spectra were acquired with a Phenon Pharos from Thermo scientific. X-ray diffraction (XRD) patterns were obtained by using an "Aeris Mineral" from Panalytical in Bragg–Brentano geometry, operating with Cu K_α radiation ($\lambda = 0.15406$ nm) generated at 40 kV and 30 mA. X-ray absorption spectroscopy (XAS) measurements were recorded on beamline B18 at Diamond Light Source (UK) with ring energy of 3 GeV and a

current of 300.[65] The monochromator used was Si(111) crystals operating in Quick EXAFS (QEXAFS) mode. Pellets of $Ni(OH)_2$ and 8Mn-$Ni(OH)_2$, and the commercial $Ni(OH)_2$ (Sigma-Aldrich) used as reference, were measured in transmission mode at the Ni K (8333 eV) and Mn K (6539 eV) absorption edges at 298 K using ion chambers. The corresponding metal foils were measured simultaneously and used for the spectra alignment. Calibration of the monochromator was carried out using the foil previously to the measurements. The acquired data were processed and analyzed using the Athena and Artemis programs, respectively. X-ray photoemission spectroscopy (XPS) measurements were acquired in a custom-made UHV system working at a base pressure of 10^{-10} mbar, equipped with an Omicron EA125 electron analyzer and an X-ray source with a dual Al − Mg anode. Core-level photoemission spectra (C 1 s, O 1 s, Mn 2p and Ni 2p) were collected at room temperature with a non-monochromatized Mg K_α X-ray source (1253.6 eV) using a 0.1 eV step, 0.5 s dwell time and pass energy 20.[66]

Electrochemical characterization: Electrochemical measurements were conducted in a three-electrode cell using a Hg/HgO electrode as a reference electrode and a graphite rod as a counter electrode. All the experiments were performed at room temperature. The working electrode was a glassy carbon (GC) electrode (3 mm diameter) modified with 5 µL of catalyst ink. The ink was prepared by mixing 3 mg of catalyst, 500 µL milli-Q water, 100 µL isopropyl alcohol, and 10 µL of Nafion® (5 wt%, Sigma-Aldrich), and sonicating until a homogeneous dispersion was formed. Previously to the GC modification with the catalyst by drop casting, it was polished with 1 µm and 0.25 µm diamond pastes and sonicated in isopropyl alcohol. Cyclic (CVs) and linear sweep voltammetries (LSVs) were acquired at 5 mV s^{-1} in N_2-saturated 1 M KOH and N_2-saturated 1 M KOH + 0.33 M urea electrolytes, prepared from high purity reagents (Sigma-Aldrich). All the LSVs reported in this work are IR corrected. The ohmic drop resistance in the solution was determined by electrochemical impedance spectroscopy (12 Ω for the 1 M KOH solution). The ohmic drop compensation was performed during the data treatment. Tafel slope values were obtained from steady state potential measurements.[67] The steady state polarization curves were constructed by sampling UOR current density at the 240th second of chronoamperometry responses acquired at various overpotentials in the catalytic turnover region with a regular interval of 0.010 V. Currents reported in the text are normalized by the electroactive surface area (ECSA), determined from the Ni^{3+}/Ni^{2+} reduction peak according to the formula: $\mathrm{ECSA} = \frac{\frac{\text{peak area}}{\text{scan rate}}}{2.75\times10^{-4}}$.[68] Potential values are referenced to the reversible hydrogen electrode (RHE) by using the following equation: $E_{RHE} = E_{Hg/HgO} + 0.098 + 0.059$ pH, where $E_{Hg/HgO}$ is the experimentally measured potential against the Hg/HgO reference electrode.

Electrochemical impedance spectroscopy (EIS) measurements were performed at open circuit voltage and at 0.55 V vs Hg/HgO in the presence of urea, over a frequency range of 100 kHz to 0.1 Hz, using a sinusoidal amplitude of 10 mV.

Rotating ring-disk electrode (RRDE) measurements were performed in the same three-electrode cell with the same experimental setup detailed above. An aliquot of 5 µL of ink was deposited by drop casting on the GC disk (5 mm diameter). LSVs were acquired on the disk at 1600 r.p.m. with a scan rate of 5 mV s^{-1} in N_2-saturated 1 M KOH and N_2-saturated 1 M KOH + 0.33 M urea, while the Pt ring potential was held at 0.4 V vs RHE. At this potential, O_2 generated by the OER can be easily reduced, while CO_2, N_2, and nitrites/nitrates generated by the UOR cannot.[69]

Urea electrolysis measurements were performed in a 50 mL gas-tight H-electrochemical cell in PEEK using a Hg/HgO electrode and a Pt wire as reference electrode and counter electrode, respectively. The Pt wire was placed in a compartment made of PEEK and separated from the main chamber through a Fumasep® FAS30 membrane previously activated in KOH for 24 h. The working electrode was prepared by spray coating onto a 2 × 1 cm^2 carbon paper. Electrolysis experiments were carried out in Ar-saturated 1 M KOH + 0.33 M urea at four different applied potentials within the UOR window (1.50–1.65 V) for 4 h (unless a charge of 30 C was reached first).

Long-term chronoamperometric measurements at 1.55 V were performed on the 8Mn-$Ni(OH)_2$ sample for 72 h, and the UOR products were determined every 24 h to study the catalytic stability and selectivity as a function of time.

Products' analysis: Gas products (N_2, O_2) formed during UOR and/or competing OER were analyzed at the end of the electrolysis tests by gas chromatography (GC, Agilent 8860 GC System) using a TCD detector. The headspace of the electrochemical cell was sampled (100 µL) with a Hamilton Syringe, and the measurement was repeated three times. Calibration curves of the two gases were obtained by diluting pure O_2 and N_2 gas in Ar flow with mass-flow controllers. Liquid products (nitrite and nitrate ions) were analyzed by ion exchange chromatography (IC) coupled to a conductivity detector (CD). The IC-CD was equipped with a pumping module (ICS-6000 SP), an eluent generator via cartridge (ICS-6000 EG), a thermostated column compartment (ICS-6000 DC), an electrochemical ion suppressor (Dionex ADRS 600 2 mm), and a conductivity detector (ICS-6000 CD). Separation was performed using an Ion-Pac AS 19–4 µm (2 × 250 mm) as an analytical column and an Ion-Pac AS 19–4 µm (2 × 50 mm) as a precolumn, both thermostated at 40 °C. The injection volume was 5 µL and the eluent flow rate was 0.2 mL min^{-1}. The mobile phase gradient profile was as follows: (t in min): t0-3, 5 mM KOH; t3-5, 5–10 mM KOH; t5-15, 10 mM KOH; t15-28, 10–70 mM KOH; t28-35, 70 mM KOH; t35-40, 70–5 mM KOH. Quantification of analytes was carried out by external calibration using a seven-point calibration curve covering the range 1–150 mg L^{-1} and proper sample dilution. Each sample was analyzed in duplicate. Linearity showed a $R^2 > 0.998$ for each analyte, and the limit of detection was 0.05 mg L^{-1}. Precision was <5%, expressed as relative standard deviation between duplicates (RSD).

Faradaic efficiency (FE) for all the products was calculated by using Equation (2),[59,62] where n_e^- is the number of transferred electrons, $n_{product}$ is the number of moles of product obtained, and Q is the charge involved in the electrolysis.[70]

$$\mathrm{FE}\ (\%) = 100 \cdot \frac{n_e^- \cdot F \cdot n_{product}}{Q}. \quad (2)$$

Density functional theory calculations: Based on XRD analysis, the experimental sample consists of a mixture of α- and β-$Ni(OH)_2$, with the β-phase being predominant. The structure of β-$Ni(OH)_2$ is determined and adopted from the literature, while the atomic structure of β-NiOOH remains unclear due to the undetermined H positions.[71–73] Several potential candidate structures of β-NiOOH have been proposed by theoretical studies, including the U, L, S, and M phases.[71,74,75] In this work, the U phase was used because previous calculations indicate that it is the most stable candidate.[36,75] Our work focuses on the (0001) facet of β-NiOOH, which is the most thermodynamically stable and abundant surface, as shown by DFT + U calculations and Wulff construction analysis in both vacuum and aqueous conditions.[75–77] We also investigated the γ-NiOOH (0001) surface as detailed in the Electronic Supporting Information (ESI).

Fully optimized structures and Urea Oxidation Reaction (UOR) activities were studied using the Heyd−Scuseria−Ernzerhof (HSE06) functional[28] augmented with D3 (BJ) corrections[29,30] as conducted in CRYSTAL17 code[68] given that previous calculations indicate hybrid functional is crucial to correctly describe the electronic structure and the related catalysis mechanism of NiOOH.[31] The Kohn–Sham orbitals were expanded using Gaussian-type orbitals with the POB-TZVP-REV2 all-electron basis sets. The energy convergence criterion was set to 10^{-6} Hartree, and a 3 × 3 × 3 k-point grid was employed. All the calculations were performed considering the spin polarization. Free energy (G) values were obtained from frequency calculations within the harmonic approximation. Table S11, Supporting Information, reports the individual energetic contributions—namely the electronic energy change (ΔE), zero-point energy change (ΔZPE), thermal contribution to the vibrational energy (ΔE), and entropic contribution ($T\Delta S$)—that together yield the total free energy change (ΔG) for each reaction step. As shown by the values reported in Table S11, Supporting Information, no significant differences are observed between the Mn-doped and undoped systems, and the overall trends in energy contributions are preserved. Further computational details are presented in the Electronic Supporting Information (ESI).

Acknowledgements

F.B. and D.C. contributed equally to this work. The authors would like to acknowledge support from the National Recovery and Resilience Plan (NRRP), by the Italian Ministry of University and Research (MUR), funded by the European Union—NextGenerationEU (P2022FALAP—CYCLE-E). The authors would like to thank the Diamond Light Source for provision of beamtime (SP19850). D.P. and C.D.V. acknowledge funding from the European Union-NextGenerationEU through the Italian Ministry of University and Research under PNRR-M4C2I1.4 ICSC-Centro Nazionale di Ricerca in High-Performance Computing, Big Data and

Quantum Computing (grant no. CN00000013). C.D.V. would like to acknowledge the National Recovery and Resilience Plan (PNRR), Mission 2 "Green Revolution and Ecological Transition," Component 2 "Renewable Energy, Hydrogen, Network and Sustainable Mobility," Investment 3.5 "Hydrogen Research and Development," European Union—Next Generation EU – Ministry of Ecological Transition, project AMBITION. Open access publishing facilitated by Universita degli Studi di Padova, as part of the Wiley - CRUI-CARE agreement.

Conflict of Interest

The authors declare no conflict of interest.

Supporting Information

Supporting Information is available from the Wiley Online Library or from the author.

Keywords

DFT calculations, energy materials, manganese doping, reaction mechanism, urea electrooxidation

Received: February 4, 2026
Revised: May 7, 2026
Published online: June 6, 2026

[1] H. Ishaq, I. Dincer, C. Crawford, *Int. J. Hydrog. Energy* **2022**, *47*, 26238.
[2] S. Y. Tee, K. Y. Win, W. S. Teo, L. D. Koh, S. Liu, C. P. Teng, M. Y. Han, *Adv. Sci.* **2017**, *4*, 1600337.
[3] M. Tahir, L. Pan, F. Idrees, X. Zhang, L. Wang, J.-J. Zou, Z. L. Wang, *Nano Energy* **2017**, *37*, 136.
[4] J. Li, Y. Ma, X. Mu, X. Wang, Y. Li, H. Ma, Z. Guo, *Adv. Sci.* **2025**, *12*, 2411964.
[5] H. Wang, X. Zheng, L. Fang, S. Lu, *ChemElectroChem* **2023**, *10*, e202300138.
[6] R. P. Forslund, C. T. Alexander, A. M. Abakumov, K. P. Johnston, K. J. Stevenson, *ACS Catal.* **2019**, *9*, 2664.
[7] X. Sun, R. Ding, *Cat. Sci. Technol.* **2020**, *10*, 1567.
[8] G. Zhan, L. Hu, H. Li, J. Dai, L. Zhao, Q. Zheng, X. Zou, Y. Shi, J. Wang, W. Hou, Y. Yao, L. Zhang, *Nat. Commun.* **2024**, *15*, 5918.
[9] J.-Y. Zhang, T. He, M. Wang, R. Qi, Y. Yan, Z. Dong, H. Liu, H. Wang, B. Y. Xia, *Nano Energy* **2019**, *60*, 894.
[10] X. Hu, J. Zhu, J. Li, Q. Wu, *ChemElectroChem* **2020**, *7*, 3211.
[11] J. Li, J. Zhang, J.-H. Yang, *Int. J. Hydrog. Energy* **2022**, *47*, 7693.
[12] S. Xu, D. Jiao, X. Ruan, Z. Jin, Y. Qiu, Z. Feng, L. Zheng, J. Fan, W. Zheng, X. Cui, *Adv. Funct. Mater.* **2024**, *34*, 2401265.
[13] Y. Yang, J. A. Yuwono, T. Whittaker, M. M. Ibáñez, B. Wang, C. Kim, A. Y. Borisevich, S. Chua, J. P. Prada, X. Wang, P. Autran, R. R. Unocic, L. Dai, A. Holewinski, N. M. Bedford, *Adv. Mater.* **2024**, *36*, 2403187.
[14] S. Lu, X. Zheng, L. Fang, F. Yin, H. Liu, *Electrochem. Commun.* **2023**, *157*, 107599.
[15] Y. Jiang, S. Gao, G. Xu, X. Song, *J. Mater. Chem. A* **2021**, *9*, 5664.
[16] Z. Li, Y. Zheng, H. Guo, X. Cheng, Y. Huang, C. Liu, J. Zang, L. Dong, *J. Alloys Compd.* **2024**, *1008*, 176591.
[17] J. Ge, J. Kuang, Y. Xiao, M. Guan, C. Yang, *Surf. Interfaces* **2023**, *41*, 103230.
[18] G. A. Volpato, A. Baciami, K. G. Kjurchieva, M. Berton, M. Schiavon, F. Bano, A. Ferrarini, S. Galvanin, D. Mosconi, J. C. Calderón, S. Pettenuzzo, E. Colusso, M. Roverso, S. Bogialli, E. Pastor, L. Calvillo, S. Agnoli, M. Cattelan, *Int. J. Hydrog. Energy* **2026**, *230*, 154696.
[19] P. Li, W. Li, Y. Huang, Q. Huang, J. Li, S. Zhao, S. Tian, *ChemSusChem* **2023**, *16*, e202201921.
[20] Q. Cao, Y. Yuan, K. Wang, W. Huang, Y. Zhao, X. Sun, R. Ding, W. Lin, E. Liu, P. Gao, *J. Colloid Interface Sci.* **2022**, *618*, 411.
[21] Q. Zhu, J. Xiao, C. Deng, H. Ding, T. Huang, G. Xu, L. Zhang, *Electrochim. Acta* **2025**, *543*, 147556.
[22] X. Yang, Y. Liu, Q. Chen, W. Yu, Q. Zhong, *Langmuir* **2024**, *40*, 24605.
[23] X. Gao, J. Dong, H. Yang, C. Ni, X. He, Z. Li, L. Tian, *J. Alloys Compd.* **2025**, *1012*, 178477.
[24] B. K. Boggs, R. L. King, G. G. Botte, *Chem. Commun.* **2009**, DOI: 10.1039/B905974A.
[25] W. Chen, L. Xu, X. Zhu, Y. Huang, W. Zhou, D. Wang, Y. Zhou, S. Du, Q. Li, C. Xie, L. Tao, C. Dong, J. Liu, Y. Wang, R. Chen, H. Su, C. Chen, Y. Zou, Y. Li, Q. Liu, S. Wang, *Angew. Chem. Int. Ed.* **2021**, *60*, 7297.
[26] D. A. Daramola, D. Singh, G. G. Botte, *Chem. Eur. J.* **2010**, *114*, 11513.
[27] L. Zhang, L. Wang, H. Lin, Y. Liu, J. Ye, Y. Wen, A. Chen, L. Wang, F. Ni, Z. Zhou, S. Sun, Y. Li, B. Zhang, H. Peng, *Angew. Chem. Int. Ed.* **2019**, *58*, 16820.
[28] Z. Zheng, D. Wu, L. Chen, S. Chen, H. Wan, G. Chen, N. Zhang, X. Liu, R. Ma, *Appl. Catal. B Environ.* **2024**, *340*, 123214.
[29] Q. Jin, M. X. Garcia-Ortiz, L. Árnadóttir, *J. Catal.* **2026**, *453*, 116503.
[30] H. Qin, Y. Ye, J. Li, W. Jia, S. Zheng, X. Cao, G. Lin, L. Jiao, *Adv. Funct. Mater.* **2023**, *33*, 33.
[31] T. Chen, J. Song, M. Xu, Z. Li, *Appl. Catal. B Environ. Energy* **2026**, *382*, 126012.
[32] M. Bersani, International Patent no. WO 2021/089403 A1. *Method for treating wastewater for the recovery of metals contained therein, and apparatus for such a method*.
[33] A. V. Krukau, O. A. Vydrov, A. F. Izmaylov, G. E. Scuseria, *J. Chem. Phys.* **2006**, *125*, 224106.
[34] S. Grimme, J. Antony, S. Ehrlich, H. Krieg, *J. Chem. Phys.* **2010**, *132*, 154104.
[35] S. Grimme, S. Ehrlich, L. Goerigk, *J. Comput. Chem.* **2011**, *32*, 1456.
[36] D. Chen, D. Perilli, R. Dronskowski, A. Selloni, C. Di Valentin, *Acta Mater.* **2025**, *299*, 121434.
[37] L. Dong, Y. Chu, W. Sun, *Chem. Eur. J.* **2008**, *14*, 5064.
[38] Y. Tang, Y. Liu, S. Yu, Y. Zhao, S. Mu, F. Gao, *Electrochim. Acta* **2014**, *123*, 158.
[39] D. S. Hall, D. J. Lockwood, C. Bock, B. R. MacDougall, *Proc. R. Soc. A Math., Phys. Eng. Sci.* **2015**, *471*, 20140792.
[40] N. A. Alhebshi, R. B. Rakhi, H. N. Alshareef, *J. Mater. Chem. A* **2013**, *1*, 14897.
[41] D. S. Hall, D. J. Lockwood, S. Poirier, C. Bock, B. R. MacDougall, *Chem. Eur. J.* **2012**, *116*, 6771.
[42] C. Mahala, M. Devi Sharma, M. Basu, *ChemElectroChem* **2019**, *6*, 3488.
[43] T.-T. Yin, H.-M. Xu, X.-L. Zhang, X. Su, L. Shi, C. Gu, S.-K. Han, *Nano Lett.* **2023**, *23*, 3259.
[44] N. Dengo, D. F. Macias-Pinilla, P. Anzini, M. Colombo, S. Virga, A. Brambilla, P. A. Zecca, D. Monticelli, F. Giannici, F. Bertolotti, *ACS Nano* **2025**, *19*, 30151.
[45] T. Tang, W.-J. Jiang, S. Niu, N. Liu, H. Luo, Y.-Y. Chen, S.-F. Jin, F. Gao, L.-J. Wan, J.-S. Hu, *J. Am. Chem. Soc.* **2017**, *139*, 8320.
[46] Z. Zhang, H. Huo, L. Wang, S. Lou, L. Xiang, B. Xie, Q. Wang, C. Du, J. Wang, G. Yin, *Chem. Eng. J.* **2021**, *412*, 128617.
[47] B. Yang, K. Li, C. Yang, Y. Zhang, Y. Gong, *Chem. Eng. J.* **2025**, *513*, 163032.
[48] Z. Liu, G. Zhang, K. Zhang, H. Lan, H. Liu, J. Qu, *J. Mater. Chem. A* **2020**, *8*, 4073.
[49] W. Yang, X. Yang, B. Li, J. Lin, H. Gao, C. Hou, X. Luo, *J. Mater. Chem. A* **2019**, *7*, 26364.
[50] M. C. Biesinger, B. P. Payne, A. P. Grosvenor, L. W. M. Lau, A. R. Gerson, R. S. C. Smart, *Appl. Surf. Sci.* **2011**, *257*, 2717.
[51] M. C. Biesinger, B. P. Payne, L. W. M. Lau, A. Gerson, R. S. C. Smart, *Surf. Interface Anal.* **2009**, *41*, 324.
[52] J. Chen, Y. Shen, *ACS Sustain. Chem. Eng.* **2024**, *12*, 5907.
[53] Y. Ma, C. Ma, Y. Wang, K. Wang, *Catalysts* **2022**, *12*, 337.
[54] V. M. Zemtsova, A. G. Oshchepkov, E. R. Savinova, *ACS Catal.* **2023**, *13*, 13466.
[55] D. Chen, F. Bano, D. Perilli, D. Mosconi, L. Litti, S. Agnoli, A. Selloni, L. Calvillo, C. Di Valentin, *Acta Mater.* unpublished.

[56] M. David, C. Ocampo-Martínez, R. Sánchez-Peña, *J. Energy Storage* **2019**, *23*, 392.
[57] W. Xu, H. Zhang, G. Li, Z. Wu, *Sci. Rep.* **2014**, *4*, 5863.
[58] J. Kim, M. Kim, S. S. Han, K. Cho, *Adv. Funct. Mater.* **2024**, *34*, 2315625.
[59] X. Gao, X. Bai, P. Wang, Y. Jiao, K. Davey, Y. Zheng, S.-Z. Qiao, *Nat. Commun.* **2023**, *14*, 5842.
[60] J. Li, J. Li, T. Liu, L. Chen, Y. Li, H. Wang, X. Chen, M. Gong, Z. Liu, X. Yang, *Angew. Chem. Int. Ed.* **2021**, *60*, 26656.
[61] J. Dabboussi, R.-A. Eichel, H. Kungl, R. Abdallah, G. Loget, *Curr. Opin. Electrochem.* **2024**, *45*, 101468.
[62] S. W. Tatarchuk, J. J. Medvedev, F. Li, Y. Tobolovskaya, A. Klinkova, *Angew. Chem.* **2022**, *134*, 134.
[63] X. Zhang, S. Feizpoor, M. Humayun, C. Wang, *Chem Catal.* **2024**, *4*, 100840.
[64] P. Wang, X. Bai, H. Jin, X. Gao, K. Davey, Y. Zheng, Y. Jiao, S. Qiao, *Adv. Funct. Mater.* **2023**, *33*, 2300687.
[65] A. J. Dent, G. Cibin, S. Ramos, A. D. Smith, S. M. Scott, L. Varandas, M. R. Pearson, N. A. Krumpa, C. P. Jones, P. E. Robbins, *J. Phys. Conf. Ser.* **2009**, *190*, 012039.
[66] B. Ravel, M. Newville, *J. Synchrotron Radiat.* **2005**, *12*, 537.
[67] S. Anantharaj, S. Noda, M. Driess, P. W. Menezes, *ACS Energy Lett.* **2021**, *6*, 1607.
[68] J. Li, S. Wang, J. Chang, L. Feng, *Adv. Powder Mater.* **2022**, *1*, 100030.
[69] H. Liu, S. Zhu, Z. Cui, Z. Li, S. Wu, Y. Liang, *Nanoscale* **2021**, *13*, 1759.
[70] N. Dutta, D. Bagchi, G. Chawla, S. C. Peter, *ACS Energy Letters* **2024**, *9*, 323.
[71] A. J. Tkalych, K. Yu, E. A. Carter, *J. Phys. Chem. C* **2015**, *119*, 24315.
[72] P. Oliva, J. Leonardi, J. F. Laurent, C. Delmas, J. J. Braconnier, M. Figlarz, F. Fievet, A. D. Guibert, *J. Power Sources* **1982**, *8*, 229.
[73] V. Y. Kazimirov, M. B. Smirnov, L. Bourgeois, L. Guerlou-Demourgues, L. Servant, A. M. Balagurov, I. Natkaniec, N. R. Khasanova, E. V. Antipov, *Solid State Ionics* **2010**, *181*, 1764.
[74] Y.-F. Li, A. Selloni, *J. Phys. Chem. Lett.* **2014**, *5*, 3981.
[75] Q. Hu, Y. Xue, J. Kang, I. Scivetti, G. Teobaldi, A. Selloni, L. Guo, L.-M. Liu, *ACS Catal.* **2022**, *12*, 295.
[76] J. M. P. Martirez, E. A. Carter, *Chem. Mater.* **2018**, *30*, 5205.
[77] Y.-F. Li, J.-L. Li, Z.-P. Liu, *J. Phys. Chem. C* **2021**, *125*, 27033.